

Electric-field-driven magnetization reversal in square-shaped nanomagnet-based multiferroic heterostructure

Ren-Ci Peng, J. J. Wang, Jia-Mian Hu, Long-Qing Chen, and Ce-Wen Nan

Citation: [Applied Physics Letters](#) **106**, 142901 (2015); doi: 10.1063/1.4917228

View online: <http://dx.doi.org/10.1063/1.4917228>

View Table of Contents: <http://scitation.aip.org/content/aip/journal/apl/106/14?ver=pdfcov>

Published by the [AIP Publishing](#)

Articles you may be interested in

[Simultaneous imaging of the ferromagnetic and ferroelectric structure in multiferroic heterostructures](#)

APL Mat. **2**, 076109 (2014); 10.1063/1.4890055

[Giant magneto-impedance effect in amorphous ferromagnetic wire with a weak helical anisotropy: Theory and experiment](#)

J. Appl. Phys. **113**, 243902 (2013); 10.1063/1.4812278

[Voltage-driven perpendicular magnetic domain switching in multiferroic nanoislands](#)

J. Appl. Phys. **113**, 194301 (2013); 10.1063/1.4804157

[Electric field modulation of magnetoresistance in multiferroic heterostructures for ultralow power electronics](#)

Appl. Phys. Lett. **98**, 222509 (2011); 10.1063/1.3597796

[Electrically controlled magnetization switching in a multiferroic heterostructure](#)

Appl. Phys. Lett. **97**, 052502 (2010); 10.1063/1.3475417

Frustrated by old technology? Is your AFM dead and can't be repaired? Sick of bad customer support?

It is time to upgrade your AFM
Minimum \$20,000 trade-in discount for purchases before August 31st

Asylum Research is today's technology leader in AFM

dropmyoldAFM@oxinst.com

OXFORD INSTRUMENTS
The Business of Science®

Electric-field-driven magnetization reversal in square-shaped nanomagnet-based multiferroic heterostructure

Ren-Ci Peng,¹ J. J. Wang,^{1,2,a)} Jia-Mian Hu,² Long-Qing Chen,^{1,2} and Ce-Wen Nan^{1,a)}

¹State Key Laboratory of New Ceramics and Fine Processing, School of Materials Science and Engineering, Tsinghua University, Beijing 100084, China

²Department of Materials Science and Engineering, The Pennsylvania State University, University Park, Pennsylvania 16802, USA

(Received 9 March 2015; accepted 28 March 2015; published online 6 April 2015)

Based on phase field modeling and thermodynamic analysis, purely electric-field-driven magnetization reversal was shown to be possible in a multiferroic heterostructure of a square-shaped amorphous $\text{Co}_{40}\text{Fe}_{40}\text{B}_{20}$ nanomagnet on top of a ferroelectric layer through electrostrain. The reversal is made possible by engineering the mutual interactions among the built-in uniaxial magnetic anisotropy, the geometry-dependent magnetic configuration anisotropy, and the magnetoelastic anisotropy. Particularly, the incorporation of the built-in uniaxial anisotropy made it possible to reverse magnetization with one single unipolar electrostrain pulse, which is simpler than previous designs involving the use of bipolar electrostrains and may alleviate ferroelectric fatigue. Critical conditions for triggering the magnetization reversal are identified. © 2015 AIP Publishing LLC. [<http://dx.doi.org/10.1063/1.4917228>]

Reversing the magnetization by means of electric fields in multiferroic magneto-electric (ME) heterostructures has attracted great attention due to its potential application in spintronic devices with low power consumption.^{1–15} In multiferroic ME heterostructures, all three possible interfacial coupling mechanisms, including charge/orbital modulation, exchange coupling, as well as elastic coupling can be utilized to reverse the local or average magnetization with electric fields. For example, in (001) BiFeO_3 -based multiferroic film heterostructures, the ferroelectric polarization \mathbf{P} favors a stripe-like domain pattern which is coupled to the magnetization \mathbf{M} in the overlying magnet through the exchange coupling mechanism, leading to an electric field-controlled net magnetization reversal.^{1–5} By controlling the magnetization precession and damping process in strain-mediated multiferroic ME heterostructures, the magnetization reversal can also be fulfilled by strain pulses induced through ferroelastic variants^{6,7} or ultrafast acoustic waves.⁸ In atomic scale magnet/ferroelectric heterostructures, the electric field can modulate the interfacial charge and orbital properties by reorienting the polarization and then reverse the magnetization locally at the interface.^{9–11} Other methods to reverse the magnetization using electric fields include models of Iwasaki,¹² Roy *et al.*,¹³ and Biswas *et al.*,¹⁴ wherein a four-fold symmetrical magnetocrystalline anisotropy, a geometry anisotropy (elliptical cylinder), and a four-electrode design were specifically needed besides the magnetoelastic anisotropy, respectively.

In our previous work, we proposed a patterned ME heterostructure of a flower-shaped single-domain Ni nanomagnet with an in-plane four-fold symmetric shape anisotropy and a ferroelectric layer underneath to achieve the electric field-controlled magnetization reversal.¹⁵ The reversal is accomplished by two successive 90° using electric fields that are generated through the synergistic actions of a

four-fold symmetrical shape anisotropy and the magnetoelastic anisotropy. Likewise, the electric field-driven magnetization reversal could also be accomplished in multiferroic heterostructures with square-patterned nanomagnets wherein the shape-induced four-fold symmetrical configuration anisotropy also exists according to the results from previous experiments and micromagnetic simulations.^{16–18} Moreover, it is easier to engineer a square-shaped nanomagnet than a flower-shaped counterpart.

This article, in the light of our previous finding,¹⁵ is aimed to explore how an electric field-controlled 180° magnetization rotation can be accomplished in a square nanomagnet-based multiferroic heterostructure using the phase field modeling and thermodynamic analysis. We chose the $\text{Co}_{40}\text{Fe}_{40}\text{B}_{20}$ (CoFeB) square nanomagnet grown on a ferroelectric (e.g., (011)-oriented $\text{Pb}(\text{Mg}_{1/3}\text{Nb}_{2/3})_{0.7}\text{Ti}_{0.3}\text{O}_3$ (PMN-PT)) single crystal as an example (see Fig. 1(a)) because CoFeB thin film is frequently applied in magnetic tunneling junctions (MTJs)^{19–22} and the (011) PMN-PT single crystal can output giant anisotropic electrostrains.^{23,24} Different from the previous preparation of the Ni/PMN-PT heterostructure, in this work, a magnetic field was applied

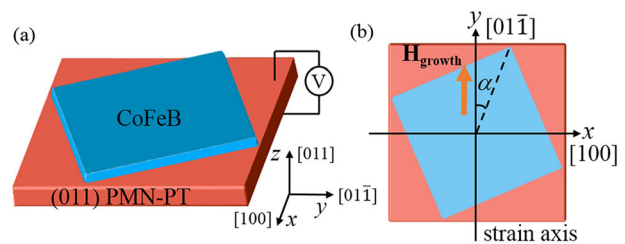


FIG. 1. (a) Schematic illustration of the multiferroic heterostructure with an amorphous CoFeB square nanomagnet grown on a (011)-PMN-PT single crystal. (b) The top view of the heterostructure where $\mathbf{H}_{\text{growth}}$, y axis, and α denote the growth field, the main direction of in-plane anisotropic piezostain, and the angle between y axis and one diagonal of the square CoFeB nanomagnet, respectively.

^{a)} Authors to whom correspondence should be addressed. Electronic addresses: jzw12@psu.edu and cwnan@tsinghua.edu.cn

during the growth process (see Fig. 1(b)) of CoFeB amorphous continuous film in order to achieve a built-in uniaxial anisotropy at first. Then, this built-in uniaxial anisotropy should remain after etching the continuous thin film into isolated nanomagnets. The purpose and results of introducing such a built-in uniaxial anisotropy will be discussed later. However, it is important to engineer the square nanomagnet to have the diagonals of the square nanomagnet to be non-collinear but to be canted with the magnetoelastic axis at a certain angle around 22° (see Fig. 1(b)).¹⁵

The phase-field modeling of the nanomagnet is same as what we used previously except that a uniaxial anisotropy energy density expressed by $f_{\text{uni}} = -K_y^{\text{growth}} m_2^2$ needs to be added into the total free energy density for incorporating the effect of the applied magnetic field along y direction during the film deposition process.¹⁵ Here, we assume that the uniaxial anisotropy of the continuous film induced by the growth field remains after the film is etched into isolated nanomagnets. The discrete grid points of $64\Delta x \times 64\Delta y \times 20\Delta z$ with a real grid space $\Delta z = 1$ nm and $\Delta x = \Delta y = 3.0$ nm are employed with the CoFeB film thickness $h_f = 5\Delta z = 5$ nm. For studying the lateral size effect, Δx was changed to achieve different sizes. The material parameters used in the simulation are found in literatures.^{25–30}

For a (011) PMN-PT single crystal under appropriate electric fields, a giant anisotropic in-plane electrostrain

($\varepsilon_y - \varepsilon_x$) up to 1500 ppm (Refs. 23 and 24) can be induced and mostly transferred to the above ultrathin (5 nm) CoFeB nanomagnet. Such an anisotropic electrostrain of 1000 ppm, as revealed in the magnetization dynamic process (see Fig. 2(a)) for a CoFeB square nanomagnet with size of 140 nm \times 140 nm \times 5 nm, can trigger the magnetization to rotate nearly 90° clockwise from the initial state^{18,19} (see state ① from 0 ns to 13 ns in Fig. 2(a) and the corresponding vector diagram in Fig. 2(b)) to state ②. Then, after the removal of the electric field and hence the volatile piezostrain becomes zero, the magnetization unexpectedly continues to rotate another 90° clockwise to state ③ (see Figs. 2(a) and 2(b)), accomplishing a 180° rotation with respect to the initial state. This 180° magnetization rotation from state ① to ③ is also repeatable, i.e., after another compressive electrostrain pulse, \mathbf{m} finishes another 180° rotation from state ③ back to state ①, as exhibited from 40 ns to 67 ns in Fig. 2(a). Moreover, this 180° rotation is nonvolatile because the final status of magnetization is stabilized by the shape and size-induced configuration anisotropy while not the electrostrain-induced magnetoelastic anisotropy.

The 180° -switching behavior of the magnetization under two successive 90° rotations can be understood through the thermodynamic energy analysis by which the Helmholtz free energy density of the proposed CoFeB nanomagnet in quasi-single-domain state is³¹

$$f^{\text{cubic}}(\mathbf{m}, \boldsymbol{\varepsilon}) = -K_1^{\text{config}}(m_1 \sin \alpha - m_2 \cos \alpha)^2(m_1 \cos \alpha + m_2 \sin \alpha) - K_y^{\text{growth}} m_2^2 + \frac{1}{2} \sum_{i,j,k,l=1}^3 c_{ijkl} (\varepsilon_{ij} - \varepsilon_{ij}^0) (\varepsilon_{kl} - \varepsilon_{kl}^0) + \frac{1}{2} \mu_0 M_S^2 (N_{11} m_1^2 + N_{22} m_2^2 + N_{33} m_3^2). \quad (1)$$

Here, the eigenstrains ε_{ij}^0 are related to the magnetostrictive coefficients according to $\varepsilon_{11}^0 = 3/2\lambda_S(m_1^2 - 1/3)$, $\varepsilon_{22}^0 = 3/2\lambda_S(m_2^2 - 1/3)$, $\varepsilon_{33}^0 = 3/2\lambda_S(m_3^2 - 1/3)$, $\varepsilon_{12}^0 = 3/2\lambda_S m_1 m_2$, ε_{13}^0

$= 3/2\lambda_S m_1 m_3$, and $\varepsilon_{23}^0 = 3/2\lambda_S m_2 m_3$. Fig. 3 shows the thermodynamic energy polar diagrams corresponding to states ①, ②, and ③ in Fig. 2(b). Initially, the magnetization is

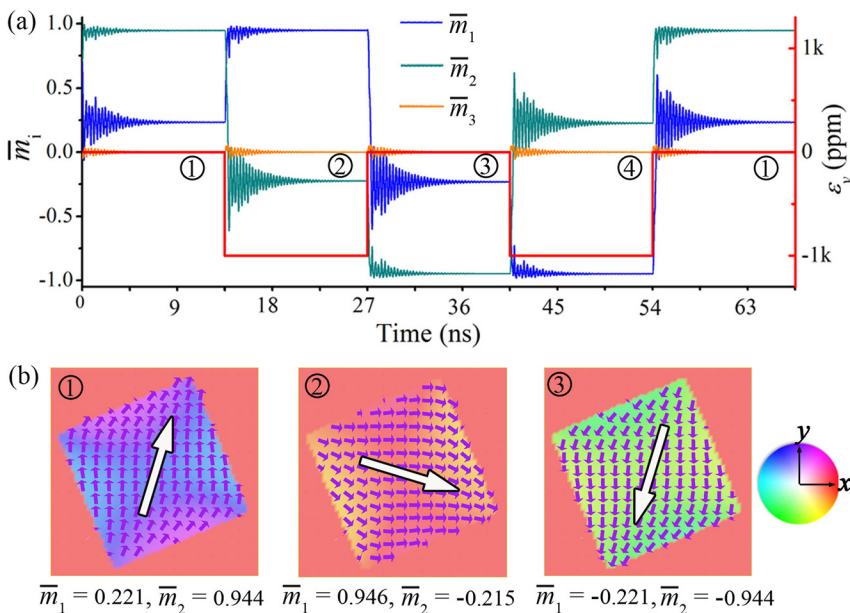


FIG. 2. (a) The dynamic process of magnetization switching driven by electric field-induced piezostrains. The time scale denotes the real time of the magnetization evolution, and the red square-wave curve represents the electric-field-induced piezostrain as a function of time. (b) The magnetization vector diagrams corresponding to some stable states of the dynamic process, in which the different background colors represent the orientations of the magnetization as indicated by the color wheel. \bar{m}_i denote the components of the average magnetization which is marked with black solid-open arrow.

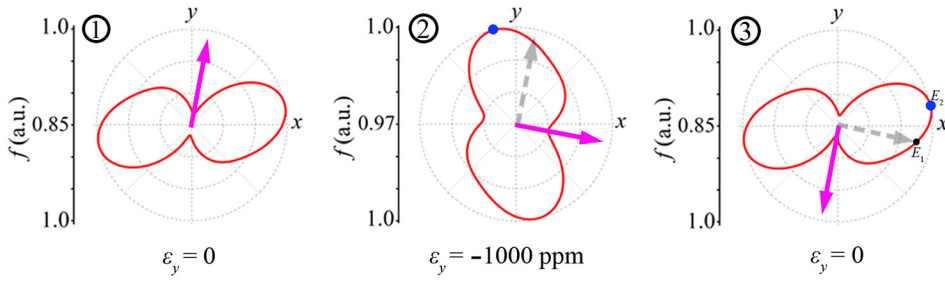


FIG. 3. Thermodynamic energy polar diagrams for states ①, ②, and ③, which explain the deterministic 180° reversal of the magnetization. The gray-dashed and magenta-solid arrows indicate the magnetization of previous and present states, respectively.

assumed to lie in the first quadrant (or the equivalent direction in the third quadrant) determined by a combination of the configuration anisotropy K_1^{config} and the built-in uniaxial anisotropy K_y^{growth} . Under an electric field-induced anisotropic electrostrain of $\varepsilon_y = -1000$ ppm, the energy polar diagram is changed, and the magnetization is switched 90° clockwise to the fourth quadrant because one of the energy maxima lies on the left of the initial magnetization direction (see the blue-solid circle and gray dashed vector on ② in Fig. 3). After the prompt removal of the piezostrain, even though the energy polar diagram is changed back to the initial state, the magnetization does not switch back but rotates another 90° clockwise to the third quadrant, as exhibited in the diagram ③ of Fig. 3 (see the blue solid circle and gray dashed vector). However, in real application, usually the removal of the stress is not abruptly but depends on the deformation response speed of the ferroelectric layer to the externally applied voltage. Accordingly, the accomplishment time of the second 90° switching from ② to ③ in order to achieve 180° rotation will depend on the stress relaxation speed of the ferroelectrics. Therefore, a reversal is accomplished under only a pure electric field-induced compressive electrostrain pulse, which is easier to be fulfilled comparing to our previous model wherein a pair of compressive and tensile strains are necessary in order to finish a 180° magnetization rotation.¹⁵ This is the reason that a magnetic field was applied during the CoFeB film growth process to introduce a uniaxial anisotropy.

The effect of this built-in uniaxial anisotropy has to conquer the effect of the configuration anisotropy to make the easy axis of the nanomagnet of two-fold symmetry, i.e., there should be only two minima on the energy polar diagram for the zero-strain state (① and ③) in order to ensure that the magnetization can rotate to the third quadrant without overcoming an energy barrier. To illustrate this, we assume that K_y^{growth} has a value of only forty percent of K_1^{config} , and meanwhile the magnetization points to the energy minimum in the fourth quadrant under a electrostrain of $\varepsilon_y = -1000$ ppm, as exhibited by the thermodynamic analysis in Fig. 4(a) and the corresponding phase-field domain vector diagram in Fig. 4(c). After the removal of the electrostrain, the energy polar diagram changes back to the unstrained case wherein there are four energy minima, leading to that \mathbf{m} rotate a small angle to the adjacent energy minimum but fails to finish an 180° rotation, as exhibited in Figs. 4(b) and 4(d). In order to satisfy the condition that there are only two minima on the energy polar diagram, the relationship between K_y^{growth} and K_1^{config} can be numerically obtained by solving the following equations requiring only two solutions for φ within $[0, 2\pi]$:

$$\begin{cases} \frac{\partial f}{\partial \varphi} = -K_1^{\text{config}} [p \cos(4\varphi) + q \sin(4\varphi)] - K_y^{\text{growth}} \sin(2\varphi) \\ \quad + \frac{3}{2} \lambda_s (c_{11} - c_{12}) (\varepsilon_{11} - \varepsilon_{22}) \sin(2\varphi) = 0 \\ \frac{\partial^2 f}{\partial \varphi^2} = K_1^{\text{config}} [4p \sin(4\varphi) - 4q \cos(4\varphi)] - 2K_y^{\text{growth}} \cos(2\varphi) \\ \quad + 3\lambda_s (c_{11} - c_{12}) (\varepsilon_{11} - \varepsilon_{22}) \cos(2\varphi) > 0, \end{cases} \quad (2)$$

where $p = 2bc(b^2 - c^2)$, $q = \frac{(b^2 - c^2)^2}{2} - 2b^2c^2$, $b = \sin \alpha$, $c = \cos \alpha$, and φ the in-plane orientation angle of \mathbf{m} ($m_1 = \cos \varphi$, $m_2 = \sin \varphi$). Fig. 4(e) shows the critical value of $K_y^{\text{growth}}/K_1^{\text{config}}$ for satisfying the condition that Eq. (2) has only two solutions with φ within $[0, 2\pi]$ interval at

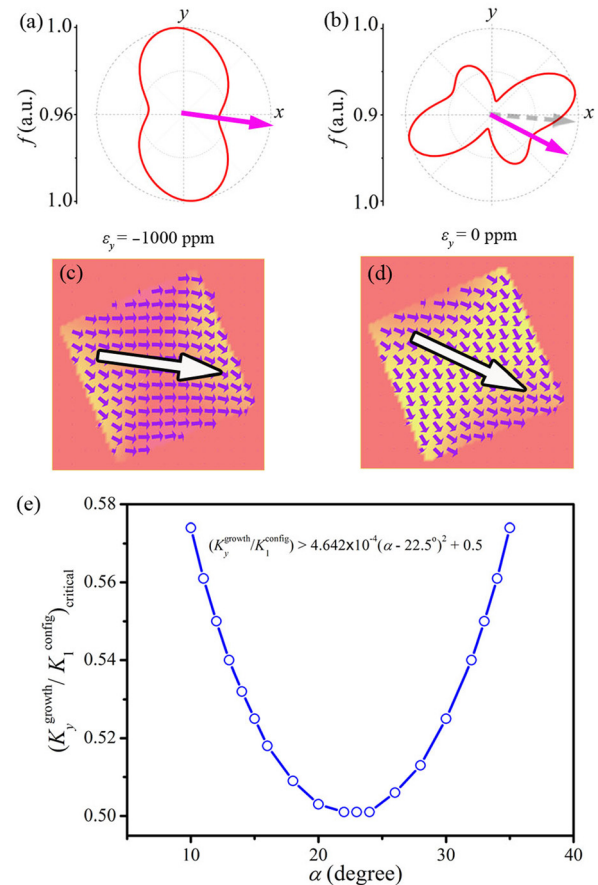


FIG. 4. Thermodynamic energy polar diagrams for CoFeB square-shaped nanomagnet with size of $140 \text{ nm} \times 140 \text{ nm} \times 5 \text{ nm}$ under (a) compressive strain of $\varepsilon_y = -1000$ ppm and (b) zero when the growth field induced uniaxial anisotropy is small ($K_y^{\text{growth}}/K_1^{\text{config}} = 0.4$), with the corresponding domain structures obtained from phase-field modeling shown in (c) and (d). (e) Tilting angle-dependent critical value of $K_y^{\text{growth}}/K_1^{\text{config}}$ for achieving the 180° magnetization switching.

$\varepsilon_{11} = \varepsilon_{22} = 0$. With the tilting angle α changing for instance from 10° to 35° , the critical value of $K_y^{\text{growth}}/K_1^{\text{config}}$ shows a parabola-like curve with a minimum of 0.5 at $\alpha = 22.5^\circ$. In order to accomplish the 180° magnetization rotation, $K_y^{\text{growth}}/K_1^{\text{config}}$ has to be stronger than the corresponding critical value at a given tilting angle α .

Now turn to another key factor for achieving the 180° magnetization rotation: the electric field-induced electrostrain has to be strong enough in order to switch the magnetization by 90° at first (namely, from state ① to state ② shown in Fig. 2). The critical strain also can be obtained by analyzing Eq. (2) in which the critical strain is related to K_y^{growth} and K_1^{config} depending on the size of the nanomagnet. As shown in Fig. 5, with the lateral size increasing from 50 nm to 180 nm, the phase field simulation shows that the K_1^{config} increases at first to a maximum of 3.6 kJ/m^3 at 110 nm and then decreases gradually, which is consistent with the experimental measurement on Supermalloy ($\text{Ni}_{80}\text{Fe}_{14}\text{Mo}_5\text{X}_1$ where X is other metals) nanomagnets.¹⁷ Meanwhile, both the phase field simulation and thermodynamic analysis show that the critical strain increases fast at first before the maximum of the configuration anisotropy and then gradually approaches to stabilization, as exhibited in Fig. 5. Note here that after the maximum of the configuration anisotropy, the critical strain obtained from phase field simulation is stronger than the result from the thermodynamic analysis, which is attributed to the increasing contribution of the exchange energy due to the larger size-induced inhomogeneous magnetization distribution with “leaf” or “flower” pattern.¹⁷ What is more, as discussed above, once removing the stress,

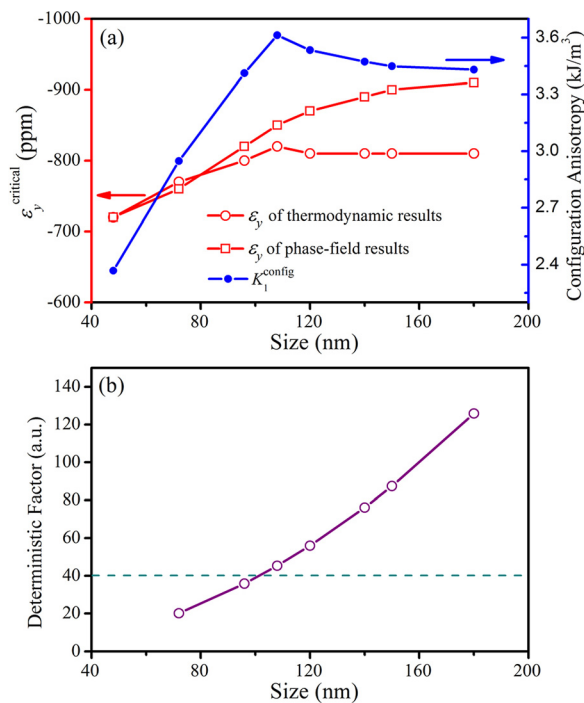


FIG. 5. Size effects (a) on the configuration anisotropy and the critical strain, (b) deterministic factor under thermal fluctuation (at 300 K) for accomplishment of 180° switching. In (a), the blue circle dot-line represents the configuration anisotropy strength obtained from the numerical solution of the magnetostatic equilibrium equation, and the red open-circle and open-square dot lines represent the critical strains obtained from the thermodynamic analysis and phase-field simulations, respectively.

the second deterministic 90° rotation from ② to state ③ is crucial for achieving the 180° magnetization switching, whereas it may be disturbed by the thermal fluctuation. The thermal stability can be evaluated by the deterministic factor which is defined as $\Delta E/k_B T$, where $\Delta E (=E_2 - E_1 = f_{\text{barrier}} V_f$, see ② in Fig. 3) is the energy barrier that determines the clockwise unidirectional rotation of magnetization and V_f indicates the volume of square nanomagnet (k_B is the Boltzmann constant and T is the temperature in Kelvin).^{15,31,32} Fig. 5(b) shows the calculated dependence of the deterministic factor on the size of nanomagnets at room temperature. In order to sustain the deterministic switching, a deterministic factor larger than 40 is necessary which means that the lateral size of the nanomagnets has to be larger than $108 \text{ nm} \times 108 \text{ nm}$, as exhibited in Fig. 5(b).

In conclusion, by employing the phase field modeling and thermodynamic analysis, we demonstrate that the electric field-controlled magnetization reversal is feasible in square-shaped CoFeB nanomagnets-based multiferroic heterostructure. In order to achieve the magnetization reversal under only a unipolar electrostrain pulse, the simulations show that the three anisotropies existing in the proposed multiferroic heterostructure have to satisfy the following conditions: (1) the built-in uniaxial anisotropy has to be stronger than at least half of the configuration anisotropy depending on the tilting angle of the nanomagnet; (2) the interfacial transferred electrostrain has to be more than a critical value depending on the lateral size of the CoFeB nanomagnet; (3) the lateral size of the nanomagnets should be large enough (at least $108 \text{ nm} \times 108 \text{ nm}$ when the thickness of CoFeB is 5 nm) to sustain the deterministic switching under thermal fluctuation. Therefore, we expect our work to attract future experimental and engineering efforts on improving the MTJ effect by utilizing the electric field-controlled 180° magnetization switching in spintronic devices based on the proposed multiferroic ME heterostructures.

This work was supported by the NSF of China (Grant Nos. 11234005, 51332001, 51472140, and 51221291), and the NSF (Grant Nos. DMR-1410714, DMR-1420620, and DMR-1210588).

¹J. T. Heron, J. L. Bosse, Q. He, Y. Gao, M. Trassin, L. Ye, J. D. Clarkson, C. Wang, J. Liu, J. Salahuddin *et al.*, *Nature* **516**, 370 (2014).

²J. J. Wang, J. M. Hu, T. N. Yang, M. Feng, J. X. Zhang, L. Q. Chen, and C. W. Nan, *Sci. Rep.* **4**, 4553 (2014).

³D. Y. Qiu, K. Ashraf, and S. Salahuddin, *Appl. Phys. Lett.* **102**, 112902 (2013).

⁴J. T. Heron, M. Trassin, K. Ashraf, M. Gajek, Q. He, S. Y. Yang, D. E. Nikonov, Y. H. Chu, S. Salahuddin, and R. Ramesh, *Phys. Rev. Lett.* **107**, 217202 (2011).

⁵Y. H. Chu, L. W. Martin, M. B. Holcomb, M. Gajek, S. J. Han, Q. He, N. Balke, C. H. Yang, D. Lee, W. Hu, Q. Zhan, P. L. Yang, A. F. Rodríguez, A. Scholl, S. X. Wang, and R. Ramesh, *Nat. Mater.* **7**, 478 (2008).

⁶J. M. Hu, T. N. Yang, J. J. Wang, H. B. Huang, J. X. Zhang, L. Q. Chen, and C. W. Nan, *Nano Lett.* **15**, 616 (2015).

⁷M. Ghidini, R. Pellicelli, J. L. Prieto, X. Moya, J. Soussi, J. Briscoe, S. Dunn, and N. D. Mathur, *Nat. Commun.* **4**, 1453 (2013).

⁸O. Kovalenko, T. Pezeril, and V. V. Temnov, *Phys. Rev. Lett.* **110**, 266602 (2013).

⁹G. Radaelli, D. Petti, E. Plekhanov, I. Fina, P. Torelli, B. R. Salles, M. Cantoni, C. Rinaldi, D. Gutierrez, and G. Panaccione, *Nat. Commun.* **5**, 3404 (2014).

- ¹⁰C. A. F. Vaz, J. Hoffman, Y. Segal, J. W. Reiner, R. D. Grober, Z. Zhang, C. H. Ahn, and F. J. Walker, *Phys. Rev. Lett.* **104**, 127202 (2010).
- ¹¹M. Fechner, P. Zahn, S. Ostanin, M. Bibes, and I. Mertig, *Phys. Rev. Lett.* **108**, 197206 (2012).
- ¹²Y. Iwasaki, *J. Magn. Magn. Mater.* **240**, 395 (2002).
- ¹³K. Roy, S. Bandyopadhyay, and J. Atulasimha, *Sci. Rep.* **3**, 3038 (2013).
- ¹⁴A. K. Biswas, S. Bandyopadhyay, and J. Atulasimha, *Appl. Phys. Lett.* **105**, 072408 (2014).
- ¹⁵J. J. Wang, J. M. Hu, J. Ma, J. X. Zhang, L. Q. Chen, and C. W. Nan, *Sci. Rep.* **4**, 7507 (2014).
- ¹⁶R. P. Cowburn, A. O. Adeyeye, and M. E. Welland, *Phys. Rev. Lett.* **81**, 5414 (1998).
- ¹⁷R. P. Cowburn, *J. Phys. D: Appl. Phys.* **33**, R1 (2000).
- ¹⁸R. P. Cowburn and M. E. Welland, *Phys. Rev. B* **58**, 9217 (1998).
- ¹⁹P. S. Li, A. T. Chen, D. L. Li, Y. G. Zhao, S. Zhang, L. F. Yang, Y. Liu, M. H. Zhu, H. Y. Zhang, and X. F. Han, *Adv. Mater.* **26**, 4320 (2014).
- ²⁰G. Q. Yu, L. T. Chang, M. Akyol, P. Upadhyaya, C. L. He, X. Li, K. L. Wong, P. K. Amiri, and K. L. Wang, *Appl. Phys. Lett.* **105**, 102411 (2014).
- ²¹H. Meng, R. Sbiaa, M. A. K. Akhtar, R. S. Liu, V. B. Naik, and C. C. Wang, *Appl. Phys. Lett.* **100**, 122405 (2012).
- ²²H. D. Gan, R. Malmhall, Z. H. Wang, B. K. Yen, J. Zhang, X. B. Wang, Y. C. Zhou, X. J. Hao, D. H. Jung, K. Satoh, and Y. M. Huai, *Appl. Phys. Lett.* **105**, 192403 (2014).
- ²³T. Wu, A. Bur, P. Zhao, K. P. Mohanchandra, K. Wong, K. L. Wang, C. S. Lynch, and G. P. Carman, *Appl. Phys. Lett.* **98**, 012504 (2011).
- ²⁴M. Buzzi, R. V. Chopdekar, J. L. Hockel, A. Bur, T. Wu, N. Pilet, P. Warnicke, G. P. Carman, L. J. Heyderman, and F. Nolting, *Phys. Rev. Lett.* **111**, 027204 (2013).
- ²⁵The material parameters including the saturated magnetization, elastic constants, magnetostrictive coefficients, Gilbert damping constant, and gyromagnetic ratio of CoFeB nanomagnet used in the simulation are as follows: $M_s = 1.0 \times 10^6$ A/m; ²⁶ $c_{11} = 2.8 \times 10^{11}$ N/m²; $c_{12} = 1.4 \times 10^{11}$ N/m²; $c_{44} = 0.7 \times 10^{11}$ N/m²; ²⁷ $\lambda_s = 3.1 \times 10^{-5}$; ²⁸ $\alpha = 0.005$; ²⁹ and $\gamma_0 = 1.76 \times 10^{11}$ Hz/T. ³⁰ The uniaxial anisotropy strength K_y^{growth} is 3.5×10^3 J/m³, and it depends on the applied magnetic field during the film deposition. The real time corresponding to each iteration step in the simulations is $\Delta T = 0.09$ ps with a τ input of 0.02.
- ²⁶C. Burrowes, N. Vernier, J.-P. Adam, L. Herrera Diez, K. Garcia, I. Barisic, G. Agnus, S. Eimer, J.-V. Kim, T. Devolder, A. Lamperti, R. Mantovan, B. Ockert, E. E. Fullerton, and D. Ravelosona, *Appl. Phys. Lett.* **103**, 182401 (2013).
- ²⁷N. A. Pertsev, *Sci. Rep.* **3**, 2757 (2013).
- ²⁸D. Wang, C. Nordman, Z. Qian, J. M. Daughton, and J. Myers, *J. Appl. Phys.* **97**, 10C906 (2005).
- ²⁹X. Liu, W. Zhang, M. J. Carter, and G. Xiao, *J. Appl. Phys.* **110**, 033910 (2011).
- ³⁰L. Q. Liu, C. F. Pai, Y. Li, H. W. Tseng, D. C. Ralph, and R. A. Buhrman, *Science* **336**, 555 (2012).
- ³¹J. J. Wang, J. M. Hu, L. Q. Chen, and C. W. Nan, *Appl. Phys. Lett.* **103**, 142413 (2013); **105**, 149901 (2014).
- ³²R. Evans, R. W. Chantrell, U. Nowak, A. Lyberatos, and H. J. Richter, *Appl. Phys. Lett.* **100**, 102402 (2012).